Ferromagnetism in DyRh and DyRhX (X = Fe, Ni, Co, Gd) thin films

Scheunert, G., Ambrose, T. F., Hendren, W. R., Lapicki, A. A., Egan, P., Hardeman, R., ... Bowman, R. M. (2014). Ferromagnetism in DyRh and DyRhX (X = Fe, Ni, Co, Gd) thin films. Journal of Physics D: Applied Physics, 47(48), [485002]. DOI: 10.1088/0022-3727/47/48/485002

Published in:
Journal of Physics D: Applied Physics

Document Version:
Peer reviewed version

Ferromagnetism in DyRh and DyRhX (X = Fe, Ni, Co, Gd) thin films

G. Scheunert[1,5]*, T. F. Ambrose[3,4], W. R. Hendren[1], A. A. Lapicki[2], P. Egan[1,2], R. Hardeman[2], M. A. Gubbins[2], and R. M. Bowman[1]

[1]Centre for Nanostructured Media, School of Mathematics and Physics, Queen's University of Belfast, Belfast BT7 1NN, UK

[2]Seagate Technology (Ireland), Springtown Industrial Estate, 1 Disc Drive, Derry BT48 0BF, UK

[3]Seagate Research (USA), 1251 Waterfront Place, Pittsburgh, PA 15222, USA

[4]Advanced Technology Laboratory, Northrop Grumman Corporation, Linthicum, MD 21090, USA

[5]Dept. of Physics of Complex Systems, Weizmann Institute of Science, 76100 Rehovot, ISRAEL

Abstract

In an effort to achieve large high-field magnetization and increased Curie temperature, polycrystalline DyRh, $(DyRh)_{95}X_5$ and $(DyRh)_{85}X_{15}$ (X = Fe, Co, Ni, Gd) thin films have been prepared via ultra-high vacuum DC co-sputtering on SiO_2 and Si wafers, using Ta as seed and cap material. A body-centred cubic CsCl-like crystal formation (B2 phase) was achieved for DyRh around the equiatomic equilibrium, known from single crystals. The maximum in-plane spontaneous magnetization at T = 4K in fields of $\mu_0 H$ = 5T of was found to be $\mu_0 M_{S,4K}$ = (1.50 ± 0.09)T with a ferromagnetic transition at T_C = (5 ± 1)K and a coercivity of $\mu_0 H_{C,4K}^{[D]}$ = (0.010 ± 0.001)T (at T = 4K) for layers deposited on substrates heated to 350°C. Samples prepared at room temperature exhibited poorer texture, smaller grains and less B2-phase content; this did impact on the Curie temperature which was higher compared to those layers with best crystallisation; however the maximal magnetization stayed unaffected. Ferromagnetic coupling was observed in ternary alloys of DyRhGd and DyRhNi with an increased Curie temperature, larger initial permeability, and

high-field magnetization which was best for $(DyRh)_{85}Gd_{15}$ with $\mu_0 M_{S,4K}^{[Gd15]}$ = (2.10 ± 0.13)T. DyRhFe and DyRhCo showed antiparallel coupling of the spontaneous magnetic moments.

Corresponding author: * gunther.scheunert@weizmann.ac.il

Introduction

Many technological applications are limited by the saturation magnetization of traditional transition-metal (TM) based magnetic materials. Consequently, there is renewed interest in alternative materials with a large saturation magnetization; one good example is the rare earth (RE) metals, particularly in alloyed form [1]. They have been considered for a multitude of applications covering magnetic refrigeration [2] [3], permanent magnets [4] [5] and superconductors [6] [7]. Finally, an area of considerable topical interest for RE-TM alloys and structures is in the study of magnetization dynamics (fast or ultrafast, laser or synchrotron based) [8], with potential applications in all-optical magnetic recording [9] [10].

Rhodates have attracted some attention for their applicability in future heat-assisted magnetic recording devices [11]; for example in FeRh thin films [12] as part of complex exchange-spring coupled magnetic recording media [13]. Furthermore, the amalgamation of REs and rhodium, such as in dysprosium-rhodium (DyRh), has been proposed as a candidate for solenoid pole pieces in thermo-electrically cooled hard disk drive write heads operating at cryogenic temperatures [14] – with a large saturation magnetization while being reasonably soft.

However, it is known from single crystals that DyRh orders ferromagnetic only below T_C = 4.8K [15], which is a severe disadvantage for application. Therefore, to increase the Curie point for tailoring a more application-suitable alloy, different ferromagnetic TMs and Gd, all with higher Curie temperatures than Dy, might be considered in ternary alloys. The understanding of the temperature-dependent magnetization of these alloys will provide a basis to identify ternary alloys with tailored characteristics.

In this paper we report on a detailed study of DyRhX (X = Fe, Ni, Co, Gd) ternary alloys around the

equiatomic DyRh composition with an atomic content of X of 5% and 15%. The films were prepared by co-sputtering, renowned for its excellent capability to create thin-film alloys of virtually any composition, even of materials which would otherwise not alloy [16].

Fabrication

Thin film of DyRh, sandwiched by 5nm Ta seed and cap layers, were prepared by direct-current (DC) magnetron-supported sputtering on Si and Si/300nm thermal SiO_2 wafers under ultra-high vacuum (UHV) conditions (base pressure < $3x10^{-9}$ mbar; argon process gas pressure = $4x10^{-3}$ mbar) using a 99.8% pure Dy, and 99.95% pure Rh and Fe targets. The sputtering targets were placed a distance of 16cm under an angle of 15° (Dy, Rh and Ta) and 25° (Fe, Ni, Co and Gd) with respect to the substrate in a Kurt J. Lesker co-sputtering device as described before [17] [18]. For the sake of better comparability we give values of deposition rates measured by a quartz crystal at a distance of 1cm to the wafer with thicknesses additionally confirmed by X-ray diffraction (XRD) and transmission electron microscopy (TEM). To aid uniformity the wafer was rotated at 20RPM. Oxygen contamination was minimised by pre-sputter of the targets (30min at 15 W/in^2) and baking the sample holder and substrate for 30min at ~350°C to allow it to outgas completely before deposition. Auger electron spectroscopy (AES) confirmed an oxygen content of less than 2%, which is the resolution limit. No Dy_2O_3 related peaks could be found in XRD Θ-2Θ scans. Ta was successfully used as a capping material to prevent further corrosion under standard atmospheric conditions as well as oxygen from the substate's oxide layer to diffuse into the magnetic layer [19] [20] [21], see figure 1 (a). The equiatomic DyRh alloy was sputtered at ~15 W/in^2 applied at each target, the equivalent of an individual sputter rate of 2.2 Å/s for Dy and 1.0 Å/s for Rh. In a first calibration series of DyRh samples around the equiatomic composition it was found that a power adjustment which would yield a composition of $Dy_{48}Rh_{52}$ results in highest saturation values for room temperature depositions. It is assumed that the actual composition is $Dy_{50}Rh_{50}$ and the deviation is due to a small misalignment of the sputtering guns. However, energy-dispersive X-ray spectroscopy (EDX) and AES as were used did not have a high enough resolution to identify a definite difference of two atomic percent in the final film, therefore sample description remains with $Dy_{48}Rh_{52}$. We present four different sample types of $Dy_{48}Rh_{52}$ thin films in this study: [A] as-

deposited, t_{DyRh} = 50nm, [B] deposited on heated wafers at 350°C, t_{DyRh} = 45nm, [C] type [B] samples subsequently post-annealed at 400°C for 2h at a base pressure of 10^{-6}mbar and [D] deposited on heated wafers at 350°C, t_{DyRh} = 75nm, to allow further crystallisation. The sample composition was verified after deposition via AES and EDX. Furthermore, two more series of (DyRh)X ternary alloys were sputtered on heated wafers at 350°C at a thickness of $t_{(DyRh)X}$ = 75nm. An addition of 5% and 15% of the third metal was chosen on the base of a calibration series of $(DyRh)_{100-Y}Fe_Y$ sputtered at room temperature, where a distinct maximum in high-field magnetization was observed for an Fe content of *Y = 15* and a distinct minimum for *Y = 5*. The first series, $(DyRh)_{95}X_5$, had a foreign atom content of 5% of X = Fe, Ni, Co and Gd; and the according samples are indexed [Fe5], [Ni5], [Co5] and [Gd5], respectively. The second series, $(DyRh)_{85}X_{15}$, had a foreign atom content of 15% and samples are indexed [Fe15], [Ni15], [Co15] and [Gd15]. A list of all samples is given in Table 1.

Si:Ta(5nm)/DyRhX/Ta(5nm)				
sample ID	**composition**	**DyRhX thickness**	**deposition temperature**	**post-anneal**
[A]	$Dy_{48}Rh_{52}$	50 nm	25°C	none
[B]	$Dy_{48}Rh_{52}$	45 nm	350°C	none
[C]	$Dy_{48}Rh_{52}$	45 nm	350°C	2h, 400°C
[D]	$Dy_{48}Rh_{52}$	75 nm	350°C	none
[Fe5]	$(Dy_{48}Rh_{52})_{95}Fe_5$	75 nm	350°C	none
[Ni5]	$(Dy_{48}Rh_{52})_{95}Ni_5$	75 nm	350°C	none
[Co5]	$(Dy_{48}Rh_{52})_{95}Co_5$	75 nm	350°C	none
[Gd5]	$(Dy_{48}Rh_{52})_{95}Gd_5$	75 nm	350°C	none
[Fe15]	$(Dy_{48}Rh_{52})_{85}Fe_{15}$	75 nm	350°C	none
[Ni15]	$(Dy_{48}Rh_{52})_{85}Ni_{15}$	75 nm	350°C	none
[Co15]	$(Dy_{48}Rh_{52})_{85}Co_{15}$	75 nm	350°C	none
[Gd15]	$(Dy_{48}Rh_{52})_{85}Gd_{15}$	75 nm	350°C	none

Table 1: Fabrication details of all DyRh and DyRhX (X = Fe, Co, Ni, Gd) samples as presented in this study.

Crystal structure analysis

A crystallographic analysis revealed a polycrystalline structure of the DyRh and DyRhX, as evident from TEM imaging, see figure 1, and XRD Θ-2Θ patterns with significant peak broadening as shown in figure 2. Single-crystal DyRh is known to order body-centred cubic (BCC), similar to CsCl in the B2 phase [22] [23], with a lattice parameter of $a^{s.c.}$ = (3.40±0.01)Å [24] [25]. Ta was chosen as a seed material for thin-film deposition not only for its excellent adhesion layer and diffusion barrier properties [21] but also for its closely matching native crystal structure: fully crystallised α-Ta orders BCC with a = 3.30Å [26]. However, thin Ta films sputtered on Si or SiO_2 wafers tend to be amorphous and possibly include traces of a body-centred tetragonal (BCT) phase with an elongated unit cell [27].

Crystal structure of DyRh

Figure 2 (a) shows Θ-2Θ scans of the DyRh samples. Pronounced peaks at 25.9°, 37.5°, 46.3° and 53.5° are consistent with the BCC (1 0 0), (1 1 0), (1 1 1) and (2 0 0) reflections of a B2 crystal structure, see also figure 1 (b). Nevertheless, the texture changes quite drastically between samples, improving for heated depositions, type [B-D], and particularly the ones which were subsequently post-annealed, type [C], as can be seen from increasing relative intensity of DyRh-related peaks. Note that in a single-element BCC crystal the (100) peak 25.9° would be forbidden and its presence represents the proper inclusion of the second element in the BCC unit cell. Furthermore, there is a shift of all DyRh-related peaks towards larger angles of films [B], [C] and [D] relative to [A], i.e. their lattice gets more and more compressed as either the film thickness or temperature of deposition increases, likely as a result of improved crystallisation, with lattice parameters closer to single-crystal values. Calculating the cubic lattice parameter from higher order (2 0 0) peaks results in $a^{[A]}$ = (3.44±0.01)Å, $a^{[B,C]}$ = (3.43±0.01)Å and $a^{[D]}$ = (3.42±0.01)Å. Using the (1 1 0) reflections

leads to values of $a^{[A]}$ = (3.42±0.01)Å, $a^{[B,C]}$ = (3.40±0.01)Å and $a^{[D]}$ = (3.38±0.01)Å. The deviation of the calculated lattice parameter obtained from the (2 0 0) and the (1 1 0) reflections indicates crystallographic strain, possibly resulting in an elongated BCT unit cell. A Scherrer analysis for grain diameter determination was applied to the (1 0 0) peak, for it is in the most suitable angular range, suggesting increasing grain sizes from type [A] to type [D] in the ~30nm range. Accuracy is limited due to the applicability of the Scherrer equation in general [28], microstrain effects, and overlapping peaks. TEM images of lamellas of all samples suggest non-spherical elongated grains with different orientation within the film, which further exacerbates the Scherrer single-peak approximation.

Crystal structure of DyRhX (X = Fe, Co, Ni, Gd)

DyRhX ternary alloys are far more complicated in their structure as shown in figure 2 (b) and (c). DyRhFe and DyRhCo samples developed an expanded DyRh lattice, particularly for higher Fe and Co content, which can be deduced from DyRh (2 0 0) and (1 1 0) peaks moving towards smaller angles. The DyRh texture is degraded for larger atomic contents of 15%, as the relative height of all peaks decreased. This difference was particularly drastic for DyRhFe and DyRhNi, where e.g. [Fe5] had much better DyRh texture than [Fe15], indicated by the intensity drop of the DyRh (0 0 2) peak. DyRhNi samples also showed reduction in the DyRh texture; however peaks evolving at 40.35° and at 42.14° (more pronounced in [Ni15]) indicate the formation of an additional phase due to Ni inclusion. With their chemical similarity, Gd and Dy have a high intersolvability and easily form alloys [29]. This is reflected in the crystallisation behaviour of DyRhGd samples, which not only show massive improvement of the RE–Rh texture (see (1 0 0) peak of [Gd5]) but another phase is formed as evident from additional peaks at 38.23° and at 55.04° for [Gd15]. As pure Gd [17], Dy [19] and also DyGd [30] alloys order hexagonally and no related peak is visible, the two peaks in [Gd15] are most likely due to the formation of GdRh, having a similar B2 structure such as DyRh however slightly different lattice parameters [31].

In-plane magnetometry

Magnetic measurements in the plane of the films were conducted with a Quantum Design MPMS XL superconducting quantum interference device (SQUID). Sample preparation and magnetometry were done in the manner described previously [17]. Following our practice for polycrystalline Dy films [19], the terminology “maximum magnetization” or “high-field (spontaneous) magnetization” is used instead of “saturation magnetization” to describe the magnetic response of the material at the maximum applied field of $\mu_0 H$ = 5T, denoted M_S. Zero-field-cooled–field-cooled (ZFC-FC) scans at $\mu_0 H$ = 0.01T were used to determine points of magnetic transitions. Those were transitions from ferromagnetism to paramagnetism, marked by a Curie temperature (T_C); transitions from antiferromagnetism to paramagnetism, marked by a Néel point (T_N); transitions from antiferromagnetism to ferromagnetism (T_M); and bifurcations of the ZFC-FC plots (T_B) due to the strong temperature dependence of the crystal anisotropy. Please note, that T_B is *not* the blocking temperature as for superparamagnetic specimen, whose common notation would be T_b.
The relative uncertainty of the magnetization values is approximately $\Delta M/M$ = 6% (discussion in [27]). The uncertainty of the temperatures is dictated by the according step size of the scan.

Magnetic properties of DyRh

High-field magnetization

Figure 3 (a) shows high-field magnetization-vs.-temperature measurements for DyRh samples type [D]. All sample types, [A-D], show similar magnetic moments and transition behaviour. In fact, high-field magnetizations are the same well within the uncertainty with $\mu_0 M_{S,4K}^{[A\text{-}D]}$ = (1.50 ±

0.09)T. This comes somewhat as a surprise, given the much better crystal structure of samples type [B-D], one would expect at least significant changes or even improved magnetization due to changes in interatomic spacing of the Dy atoms. To adequately compare magnetic moments to literature, magnetization shall be given in units of Bohr magnetons per atom. In order to do so, a simplification is necessary: assuming the DyRh thin films order pseudo-single crystal, i.e. as a perfect B2 phase material with the lattice parameter a = 3.43Å, in which the embedded Dy atoms form a simple cubic sublattice. Only the Dy atoms get assigned an effective moment neglecting possible polarisation of Rh atoms. High-field magnetization measurements yield $m_{film} = 5.1\mu_B$, which is significantly reduced compared to previous studies on DyRh single crystals, reporting an effective high-field moment of $m_{bulk} = 6.4\mu_B$ [15].

There are a number of possible explanations for the observed reduction in effective moment. Firstly, there is the influence of grain boundaries between DyRh crystals in the thin film on the magnetic ordering. RE metals are particularly sensitive to changes in interatomic spacing [32], hence crystalline material tends to suffer from reduced high-field magnetization for they often do not fully saturate [33] and, for Gd antiparallel coupling of adjacent atoms in the grain boundary region [34] was found to have negative impact, too. Secondly, there is a stressed lattice, which can have similar diminishing impact on magnetization due to a change in interatomic spacing, as for pure Dy [19]. Furthermore, XRD scans as well as TEM images suggest elongated grains with different orientation within the film, i.e. the DyRh is far from the above assumption of ordering nicely single-crystal throughout the entire layer. Thirdly, although too small to quantify properly, AES indicated traces of O_2 in the films and thus it is possible that Dy_2O_3 is present in quantities too small to be seen in any XRD spectra, and this would also contribute to a reduction in magnetization.

ZFC-FC scans and magnetic structure

ZFC-FC scans of all four sample types looked qualitatively similar to the one presented in figure 3

(b), with a bifurcation at $T_B^{[A]}$ = (11 ± 1)K, $T_B^{[C]}$ = (10 ± 1)K and $T_B^{[D]}$ = (7 ± 1)K for type [A], [C] and [D] films, respectively. This might be a result of different phases in the material having different crystal anisotropies, i.e. with further crystallisation into the pure DyRh phase the bifurcation moves closer to the Curie temperature (as for type [D]) and eventually disappears. Considering the large crystal anisotropy of pure Dy, superparamagnetism seems an unlikely reason for the bifurcation, however cannot entirely be excluded, since the coercivity of DyRh was much lower, which will be discussed below. The Curie temperature was deduced from $1/\chi$ plots of ZFC branches as shown in figure 3 (c) and was also found to gradually decrease from type [A] to type [D] samples (i.e. with further crystallisation of the DyRh phase): $T_C^{[A]}$ = (9 ± 1)K, $T_C^{[C]}$ = (7 ± 1)K and $T_C^{[D]}$ = (5 ± 1)K. The latter is consistent with single-crystal values of $T_C^{s.c.}$ = (4.8 ± 0.5)K [15]. The deviation of the $1/\chi$ plot for $T > T_C$ from paramagnetic behaviour suggests ferrimagnetic coupling of (at least) two different magnetic phases and was particularly pronounced for room temperature depositions, type [A], with poorest DyRh texture, supporting the idea of multiple phases.

Hysteresis loops and coercivity

The strong influence of the grain size is reflected in the coercive field strength $H_{C,4K}$ (measured at T = 4K) which decreases with increasing grain diameter, $\mu_0 H_{C,4K}^{[A]}$ = (0.035 ± 0.002) T, $\mu_0 H_{C,4K}^{[C]}$ = (0.023 ± 0.001)T, $\mu_0 H_{C,4K}^{[D]}$ = (0.010 ± 0.001)T, and is smallest for type [D] films with best crystallisation of the DyRh phase as can be seen from hysteresis loops shown in figure 3 (d). Therefore, DyRh is one of very few RE-TM alloys which are reasonably soft in their crystalline state.

Magnetic properties of DyRhX (X = Fe, Co, Ni, Gd)

High-field magnetization of $(Dy_{48}Rh_{52})_{95}X_5$ and $(Dy_{48}Rh_{52})_{85}X_{15}$

The development of the high-field magnetization for DyRhX ternary alloys is shown in figure 4 (a) and (b). DyRhFe thin films, [Fe5] and [Fe15], follow the trend of initial calibration depositions at room temperature: there is an increase in magnetization for [Fe5] of $\mu_0 M_{S,4K}^{[Fe5]}$ = (1.70 ± 0.10)T and it drops for higher Fe content again to the DyRh level of $\mu_0 M_{S,4K}^{[Fe15]}$ = (1.50 ± 0.09)T. The small increase for [Fe5] might be a result of the stabilisation of the DyRh texture: all three DyRh-related peaks in the XRD spectra in figure 2 (b) are clearly more pronounced for [Fe5] than those of [Fe15] in figure 2 (c). DyRhCo shows a small drop in magnetization for [Co5] with $\mu_0 M_{S,4K}^{[Co5]}$ = (1.40 ± 0.08)T and also returns to DyRh values for [Co15] $\mu_0 M_{S,4K}^{[Co15]}$ = (1.50 ± 0.09)T. DyRhNi jumps to $\mu_0 M_{S,4K}^{[Ni5,Ni15]}$ = (1.70 ± 0.10)T for both compositions. DyRhGd might be considered the most interesting candidate as there is a steady increase in magnetization with increasing Gd content, $\mu_0 M_{S,4K}^{[Gd5]}$ = (1.80 ± 0.11)T up to $\mu_0 M_{S,4K}^{[Gd15]}$ = (2.10 ± 0.13)T, possibly as a result of the formation and further crystallisation of the above proposed GdRh phase.

ZFC-FC scans and magnetic structure of $(Dy_{48}Rh_{52})_{85}X_{15}$

ZFC-FC scans in applied fields of $\mu_0 H$ = 0.01T were taken for $(Dy_{48}Rh_{52})_{85}X_{15}$, shown in figure 4 (c) and (d). Those scans indicate the complex magnetic structure of the ternary alloys. $1/\chi$ plots were used to determine bifurcation and Néel temperatures as well as further magnetic transitions: $T_B^{[Fe15]}$ = (70 ± 3)K, $T_B^{[Co15]}$ = (61 ± 3)K, $T_B^{[Ni15]}$ = (28 ± 3)K, $T_B^{[Gd15]}$ = (40 ± 2)K; $T_N^{[Fe15]}$ = (58 ± 3)K, $T_N^{[Co15]}$ = (52 ± 3)K; $T_M^{[Fe15,Co15]}$ = (34 ± 3)K; $T_C^{[Ni15]}$ = (22 ± 3)K, $T_C^{[Gd15]}$ = (10 ± 3)K.

The above ZFC-FC results indicate antiparallel coupling of the magnetic TM and Dy in [Fe15] and [Co15], giving rise to what appears to be an antiferromagnetic phase, which matches expectations arising from the reduced high-field magnetizations (see figure 4 (b)). Transitions at $T_M^{[Fe15,Co15]}$ (a local magnetization minimum in the ZFC branch) are the turning point below which DyRh seems to dominate the magnetic behaviour of the specimen: in similar ZFC-FC plots for pure type [D] DyRh

in figure 3 (b) the magnetization of DyRh drops to zero at $T \approx 30$K. Comparatively sharp peaks in the ZFC-FC plots at $T_N^{[Fe15]}$ and $T_N^{[Co15]}$ are reminiscent of Néel points, which indicate a transition from antiferromagnetism to ferromagnetism. This strongly suggests that there are a larger number of magnetic phases involved, beyond simple DyRh and pure Fe or Co, whose magnetic moments nevertheless do couple antiparallel. Another possible interpretation of the ZFC-FC plots in figure 4 (c) would be an asperomagnetic magnetic structure – known from for instance pure Dy, whose ZFC-FC plots look qualitatively similar, yet which has different transition temperatures [19].

Dy and Gd in [Gd15] thin films show indications of parallel coupling, which results in ferromagnetic behaviour with much larger initial permeability and softness than [Fe15] and [Co15]. This becomes visible in larger magnetizations in the FC branches in figure 4. ZFC-FC plots of [Ni15] alloys show rather surprising ferromagnetism, where one would expect ferrimagnetism or more complex magnetic ordering, such as for [Fe15] and [Co15], due to antiparallel coupling of Ni and Dy. Although higher than for [Fe15] and [Co15], the high-field magnetization in figure 4 (b) still does not match full ferromagnetic coupling. A possible explanation might be a significant phase separation of Ni, allowing the creation of ferromagnetic Ni or NiRh clusters (or another type of a separated phase such as a layer). These have inner parts which are separated well enough, and hence do not couple antiparallel to the Dy in the DyRh matrix, but act as isolated ferromagnetic "islands". The idea of a separate phase finds support in the increased softness of [Ni15], compared to [Fe15] or [Co15], which can be seen in the much larger magnetization values in FC scans in figure 4 (d), close to those of ferromagnetic [Gd15], and a lower bifurcation temperature. Another indication for the formation of a separate phase is given by additional peaks in the XRD spectrum of DyRhNi alloys, [Ni5] and [Ni15], in figure 2, which evolve for larger Ni content. However the Θ-2Θ scans are far from drawing a complete picture and no decisive answer to crystal structure and magnetic ordering of [Ni15] can be given here.

Summary and Outlook

DyRh layers, sandwiched by Ta, sputtered on SiO_2 and Si wafers at room temperature and 350°C, of high purity were obtained, as confirmed by AES and TEM EDX. A B2-phase ordering with slightly strained lattice parameters compared to single crystals was found via XRD Θ-2Θ scans, where texture improved significantly for heated depositions and also improved for thicker layers. The in-plane high-field magnetization of $\mu_0 M_{S,4K}^{[A\text{-}D]} = (1.50 \pm 0.09)$T was independent of the texture, whereas the Curie temperature gradually decreased with further crystallisation into the B2 phase until it reached single-crystal values of $T_C^{[D]} = (5 \pm 1)$K. Those thicker films sputtered at 350°C were also the softest with a coercivity of $\mu_0 H_{C,4K}^{[D]} = (0.010 \pm 0.001)$T, which gives DyRh an outstanding position among well-crystallised RE-TM alloys which tend to be rather hard.

Ternary DyRhX alloys of $(Dy_{48}Rh_{52})_{95}X_5$ and $(Dy_{48}Rh_{52})_{85}X_{15}$ (X = Fe, Co, Ni, Gd) were co-sputtered at elevated temperatures of 350°C and characterised in a similar fashion. For a foreign atom content of 5%, antiparallel coupling of the Co to the Dy lead to an overall moment reduction; whereas the high-field magnetization slightly increased for Fe, perhaps due to the stabilisation of the DyRh phase (although texture improvement of pure DyRh did not yield increased M_S); also for Gd, due to parallel coupling to Dy; and for Ni, despite any improvement of the DyRh texture. For 15% foreign atom content, antiparallel coupling of Fe and Co to the Dy was observed, whereas Gd coupled parallel, yielding highest magnetization of $\mu_0 M_{S,4K}^{[Gd15]} = (2.10 \pm 0.13)$T, and was softer. $(Dy_{48}Rh_{52})_{85}Ni_{15}$ was also softer than $(Dy_{48}Rh_{52})_{85}Fe_{15}$, $(Dy_{48}Rh_{52})_{85}Co_{15}$ and had improved high-field magnetization over pure DyRh of $\mu_0 M_{S,4K}^{[Ni5,Ni15]} = (1.70 \pm 0.10)$T, which might be a result of the formation of another Ni-based ferromagnetic phase which is sufficiently separated from the DyRh and thus does not couple antiparallel to it. Another advantage of $(Dy_{48}Rh_{52})_{85}Ni_{15}$ and $(Dy_{48}Rh_{52})_{85}Gd_{15}$ is their larger initial permeability compared to $(Dy_{48}Rh_{52})_{85}Fe_{15}$, $(Dy_{48}Rh_{52})_{85}Co_{15}$

and even pure DyRh, which is desirable for applications such as magnetic recording.

For further clarification of how the foreign atoms are precisely implemented in the DyRh lattice and how they couple to the RE moments, X-ray magnetic circular dichroism (XMCD) measurements could be compared to *ab-initio* calculations.

Acknowledgements

We thank Seagate Technology (Ireland) for their financial support to establish ANSIN (www.ansin.eu) and help with TEM and AES measurements. We also would like to thank Dan Oron (Weizmann Institute of Science) for his support which allowed us to publish our results.

References

[1] Gutfleisch O, Willard M A, Brueck E, Chen C H, Sankar S G and Liu J P 2011 Magnetic Materials and Devices for the 21st Century: Stronger, Lighter, and More Energy Efficient *Adv. Mater.* **23** 821

[2] Gschneidner Jr. K A, Pecharsky V K and Tsokol A O 2005 Recent developments in magnetocaloric materials *Rep. Prog. Phys.* **68** 1479

[3] Shen B G, Sun J R, Hu F X, Zhang H W and Cheng Z H 2009 Recent progress in exploring magnetocaloric materials *Adv. Mater.* **21** 4545

[4] Kronmueller H 2007 *Handbook of magnetism and advanced magnetic materials* vol 4, ed S Parkin (Pennsylvania State University: John Wiley & Sons)

[5] Sugimoto S 2011 Current status and recent topics of rare-earth permanent magnets *J. Phys. D: Appl. Phys.* **44** 064001

[6] Ivanovskii A L 2008 New high-temperature superconductors based on rare-earth and transition metal oxyarsenides and related phases: synthesis, properties and simulations *Phys.-Usp.* **51** 1229

[7] Henggeler W and Furrer A 1998 Magnetic excitations in rare-earth-based high-temperature superconductors *J. Phys.: Condens. Matter* **10** 2579

[8] Radu I, Vahaplar K, Stamm C, Kachel T, Pontius N, Dürr H A, Ostler T A, Barker J, Evans R F L, Chantrell R W, Tsukamoto A, Itoh A, Kirilyuk A, Rasing T and Kimel A V 2011 Transient ferromagnetic-like state mediating ultrafast reversal of antiferromagnetically coupled spins *Nature* **472** 205–8

[9] Stanciu C D, Hansteen F, Kimel A V, Kirilyuk A, Tsukamoto A, Itoh A and Rasing T 2007 All-Optical Magnetic Recording with Circularly Polarized Light *Phys. Rev. Lett.* **99** 047601

[10] Hendren W R, Atkinson R, Pollard R J, Salter I W, Wright C D, Clegg W W and Jenkins D F L 2003 Optical and magneto-optical characterization of TbFeCo and GdFeCo thin films for highdensity recording *J. Phys.: Condens. Matter* **15** 1461

[11] Kryder M H, Gage E C, McDaniel T W, Challener W A, Rottmayer R E, Ju G, Hsia Y-T and Erden M F 2008 Heat Assisted Magnetic Recording *Proceedings of the IEEE* **96** 1810

[12] Inoue S, Ko H Y Y and Suzuki T 2008 Magnetic properties of single-crystalline FeRh alloy thin films *IEEE Trans. Magn.* **44** 2875

[13] Thiele J-U, Maat S and Fullerton E E 2003 FeRh/FePt exchange spring films for thermally assisted magnetic recording media *Appl. Phys. Lett.* **82** 2859–61

[14] Ambrose T F 2006 Magnetic write head with thermoelectric cooling device

[15] Chamard-Bois R, Van Nhung N and Pierre J 1972 Propriétés magnétiques des composés équiatomiques terres rares rhodium TRh (T = Tb, Dy, Ho, Er) *phys. stat. sol. (b)* **49** 161

[16] Gadioli G Z, Rouxinol F P, Gelamo R V, dos Santos A O, Cardoso L P and Bica de Moraes M A 2008 Magnetism in Gd-W films *J. Appl. Phys.* **103** 093916

[17] Scheunert G, Ward C, Hendren W R and Bowman R M 2012 Magnetization of 2.6T in gadolinium thin films *Appl. Phys. Lett.* **101** 142407

[18] Ward C, Scheunert G, Hendren W R and Bowman R M 2013 Realizing the high moment in Fe/Cr/Gd: the role of the rare earth *Appl. Phys. Lett.* **102** 092403

[19] Scheunert G, Hendren W R, Lapicki A A, Hardeman R, Gubbins M and Bowman R M 2013 Improved magnetization in sputtered dysprosium thin films *J. Phys. D: Appl. Phys.* **46** 152001

[20] Schauer A and Roschy M 1972 R.F. sputtered beta-tantalum and B.C.C tantalum films *Thin Solid Films* **12** 313

[21] Molarius J M T, Suni I, Laurila T, Zeng K and Kivilahti J K 1999 R.F.-sputtered tantalum-based diffusion barriers between copper and silicon *Superficies y Vacio* **9** 206

[22] Belakhovsky M and Ray D K 1975 Studies on the electronic structure of some cubic intermetallic compounds of dysprosium following the self-consistent augmented-plane-wave method *Phys. Rev. B* **12** 3956

[23] Belakhovsky M, Pierre J and Ray D K 1975 Theoretical study of the electronic structure of some cubic intermetallic compounds of dysprosium using the augmented plane wave method *J. Phys. F: Met. Phys.* **5** 2274
[24] Dwight A E, Conner R A and Downey J W 1965 Equiatomic compounds of the transition and lanthanide elements with Rh, Ir, Ni and Pt *Acta Cryst.* **18** 835
[25] Chamard-Bois R, van Nhung N, Yakinthos J and Wintenberger M M 1972 Structures magnetiques des composes equiatomiques terres rares-rhodium T Rh(T = Dy, Ho, Er) *Solid State Communications* **10** 685–9
[26] Face D W and Prober D E 1987 Nucleation of body-centered cubic tantalum films with a thin niobium underlayer *J. Vac. Sci. Technol. A* **5** 3408
[27] Scheunert G, Ward C, Hendren W R, Lapicki A A, Hardeman R, Mooney M, Gubbins M and Bowman R M 2014 Influence of strain and polycrystalline ordering on magnetic properties of high moment rare earth metals and alloys *J. Phys. D: Appl. Phys.* **47** 415005
[28] Jiang H G, Ruehle M and Lavernia E J 1999 On the applicability of the x-ray diffraction line profile analysis in extracting grain size and microstrain in nanocrystalline materials *J. Mater. Res.* **14** 549
[29] Jensen J and Mackintosh A R 1991 *Rare Earth Magnetism - Structures and Excitations* (Oxford: Clarendon Press)
[30] Levitin R Z, Perekalina T M, Shlyakhina L P, Chistyakov O D and Yakovenko V L 1973 Nature of magnetic anisotropy of dysprosium. Paramagnetic susceptibility of dysprosium-gadolinium alloys *Soviet Physics JETP* **36** 742
[31] Wang C L, Zou J D, Liu J, Mudryk Y, Gschneidner, Jr. K A, Long Y, Smetana V, Miller G J and Pecharsky V K 2013 Crystal structure, magnetic properties, and the magnetocaloric effect of Gd5Rh4 and GdRh *J. Appl. Phys.* **113** 17A904
[32] Hughes I D, Daene M, Ernst A, Hergert W, Lueders M, Poulter J, Staunton J B, Svane A, Szotek Z and Temmerman W M 2007 Lathanide contraction and magnetism in the heavy rare earth elements *Nature* **446** 650
[33] Stepankin V 1995 Magnetically aligned polycrystalline dysprosium as ultimate saturation ferromagnet for high magnetic field polepieces *Physica B* **211** 345
[34] Yue M, Zhang J X, Zeng H and Wang K J 2006 Preparation, microstructure, and magnetic properties of bulk nanocrystalline Gd metal *Applied Physics Letters* **89** 232504

Figure Captions:

FIGURE 1:

TEM imaging of type [A] Ta(5nm)/$Dy_{48}Rh_{52}$/Ta(5nm) trilayers: (a) side view of a lamella of a trilayer sputtered on a Si wafer; and (b) diffraction pattern of a trilayer sputtered on a SiN window (electron beam normal to the surface) with indexed DyRh reflection rings.

FIGURE 2:

XRD spectra of Θ-2Θ scans of Ta(5nm)/$Dy_{48}Rh_{52}$(~50nm)/Ta(5nm) trilayers sputtered on Si wafers, graph (a), Ta(5nm)/$(Dy_{48}Rh_{52})_{95}X_5$(75nm)/Ta(5nm) trilayers, and Ta(5nm)/$(Dy_{48}Rh_{52})_{85}X_{15}$(75nm)/Ta(5nm) trilayers, graph (c). Note, peaks of the Si wafer and the Ta (seed and cap) are not indexed.

FIGURE 3:

In-plane magnetization-vs.-temperature scans of type [D] DyRh: (a) High-field magnetization scan including subsequent recording of the remnant magnetization M_{rem} in zero field; and (b) ZFC-FC scan ($\mu_0 H$ = 0.01T). Graph (c) shows a typical ZFC $1/\chi$ plot from which the Curie temperature was deduced. Graph (d) shows hysteresis loops of sample types [A,C,D] recorded at T = 4K with a maximum applied field strength of $\mu_0|H_{max}|$ = 1T, shown in the inset for type [D].

FIGURE 4:

In-plane magnetization-vs.-temperature scans of DyRhX (X = Fe, Ni, Co, Gd) ternary alloys with an X content of 5% and 15%. Graph (a) shows high-field magnetization data for $(DyRh)_{95}X_5$ samples, graph (b) for $(DyRh)_{85}X_{15}$. Graphs (c) and (d) depict ZFC(→)–FC(←) scans of $(DyRh)_{85}X_{15}$ samples ($\mu_0 H$ = 0.01T).

FIGURE 1:

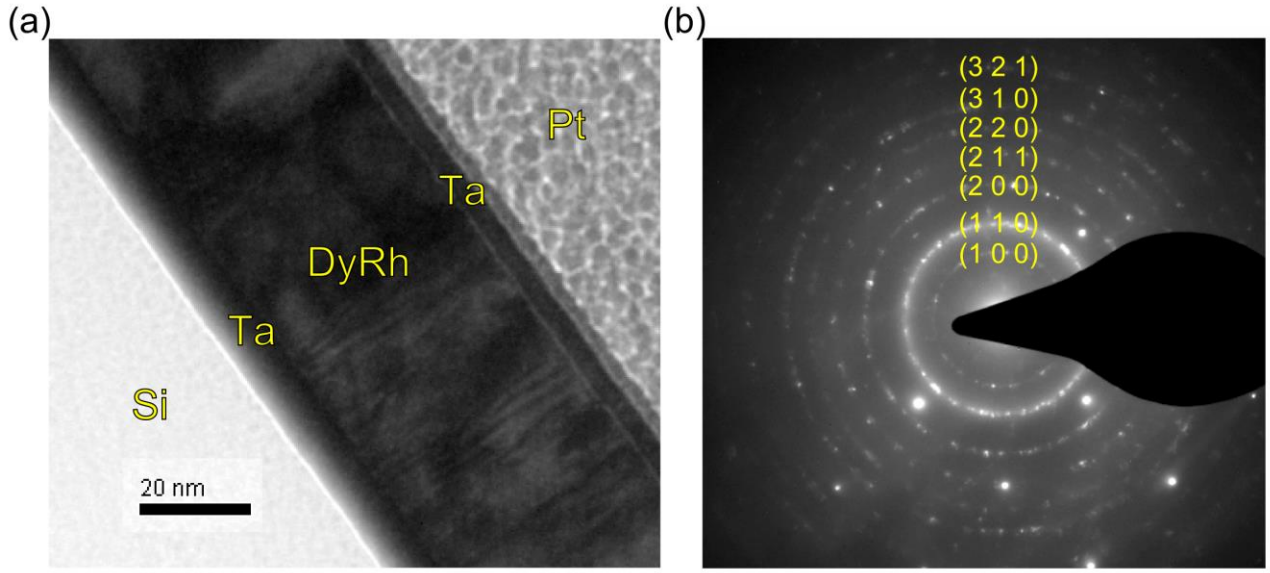

FIGURE 2:

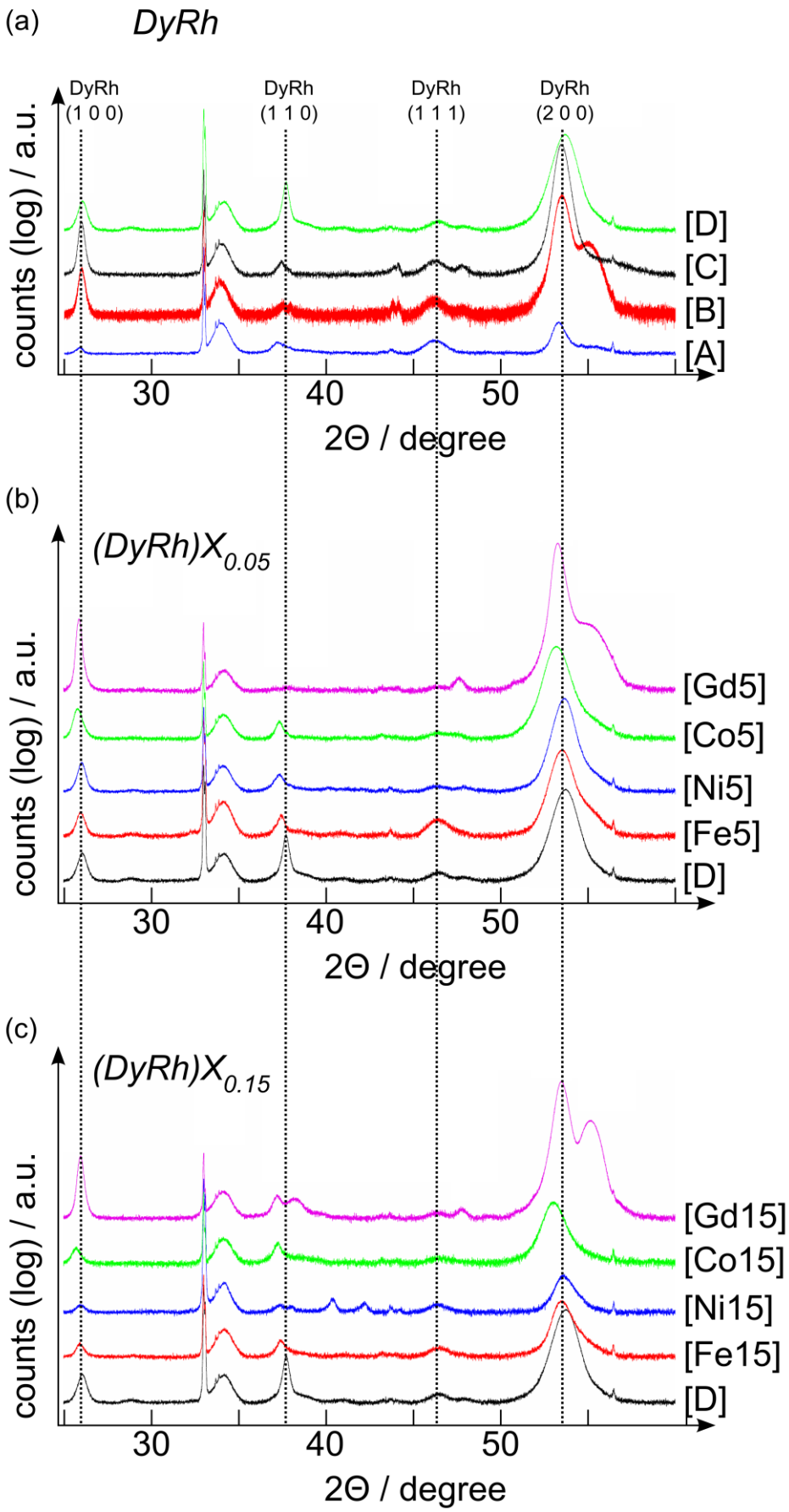
(a)
DyRh
DyRh (1 0 0)
DyRh (1 1 0)
DyRh (1 1 1)
DyRh (2 0 0)
counts (log) / a.u.
[D]
[C]
[B]
[A]
30
40
50
2Θ / degree
(b)
(DyRh)X0.05
counts (log) / a.u.
[Gd5]
[Co5]
[Ni5]
[Fe5]
[D]
30
40
50
2Θ / degree
(c)
(DyRh)X0.15
counts (log) / a.u.
[Gd15]
[Co15]
[Ni15]
[Fe15]
[D]
30
40
50
2Θ / degree

FIGURE 3:

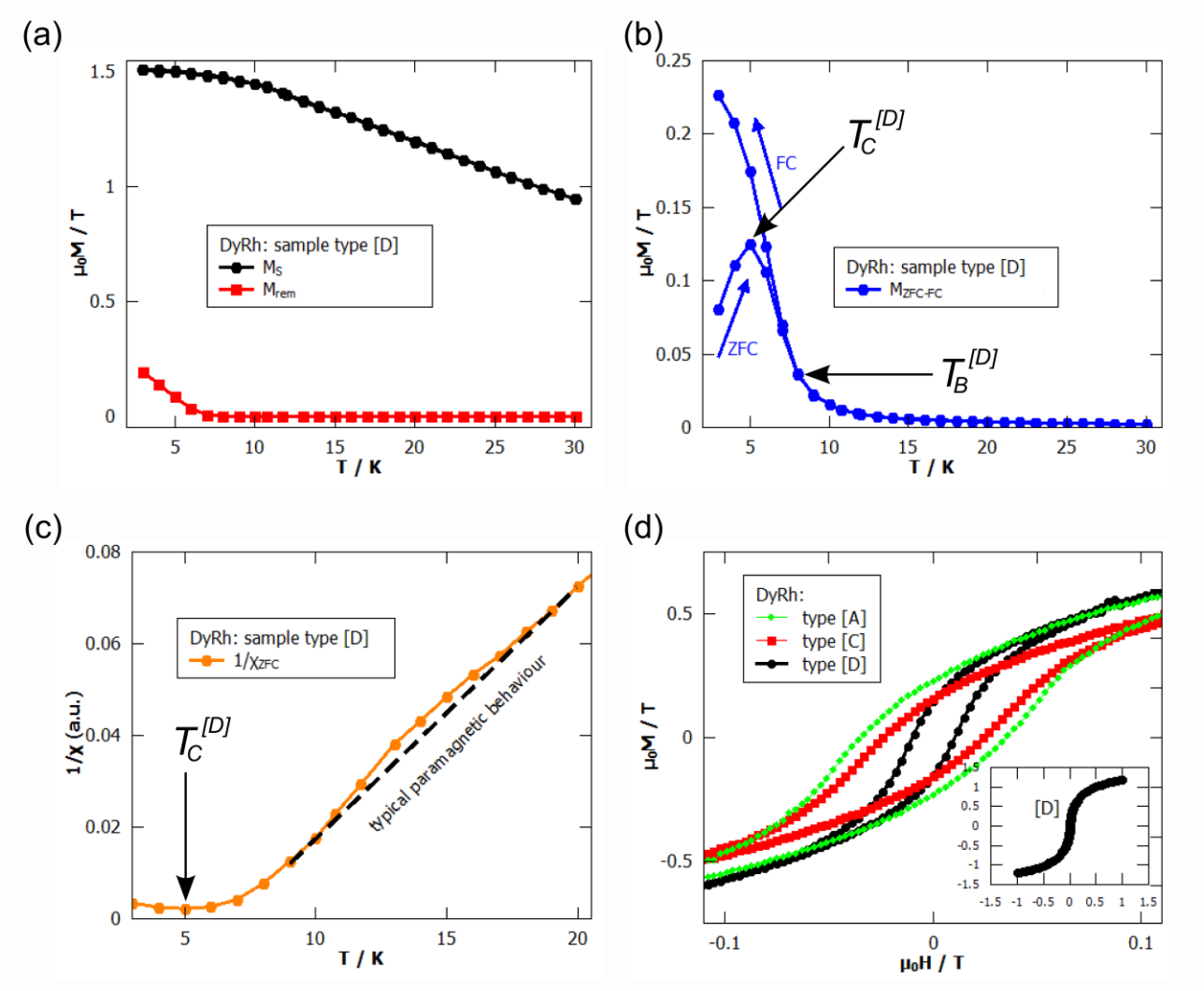
(a)
DyRh: sample type [D]
M_S
M_{rem}
$\mu_0 M$ / T
T / K
(b)
FC
ZFC
$T_C^{[D]}$
$T_B^{[D]}$
DyRh: sample type [D]
M_{ZFC-FC}
$\mu_0 M$ / T
T / K
(c)
DyRh: sample type [D]
$1/\chi_{ZFC}$
$T_C^{[D]}$
typical paramagnetic behaviour
1/χ (a.u.)
T / K
(d)
DyRh:
type [A]
type [C]
type [D]
[D]
$\mu_0 M$ / T
$\mu_0 H$ / T

FIGURE 4:

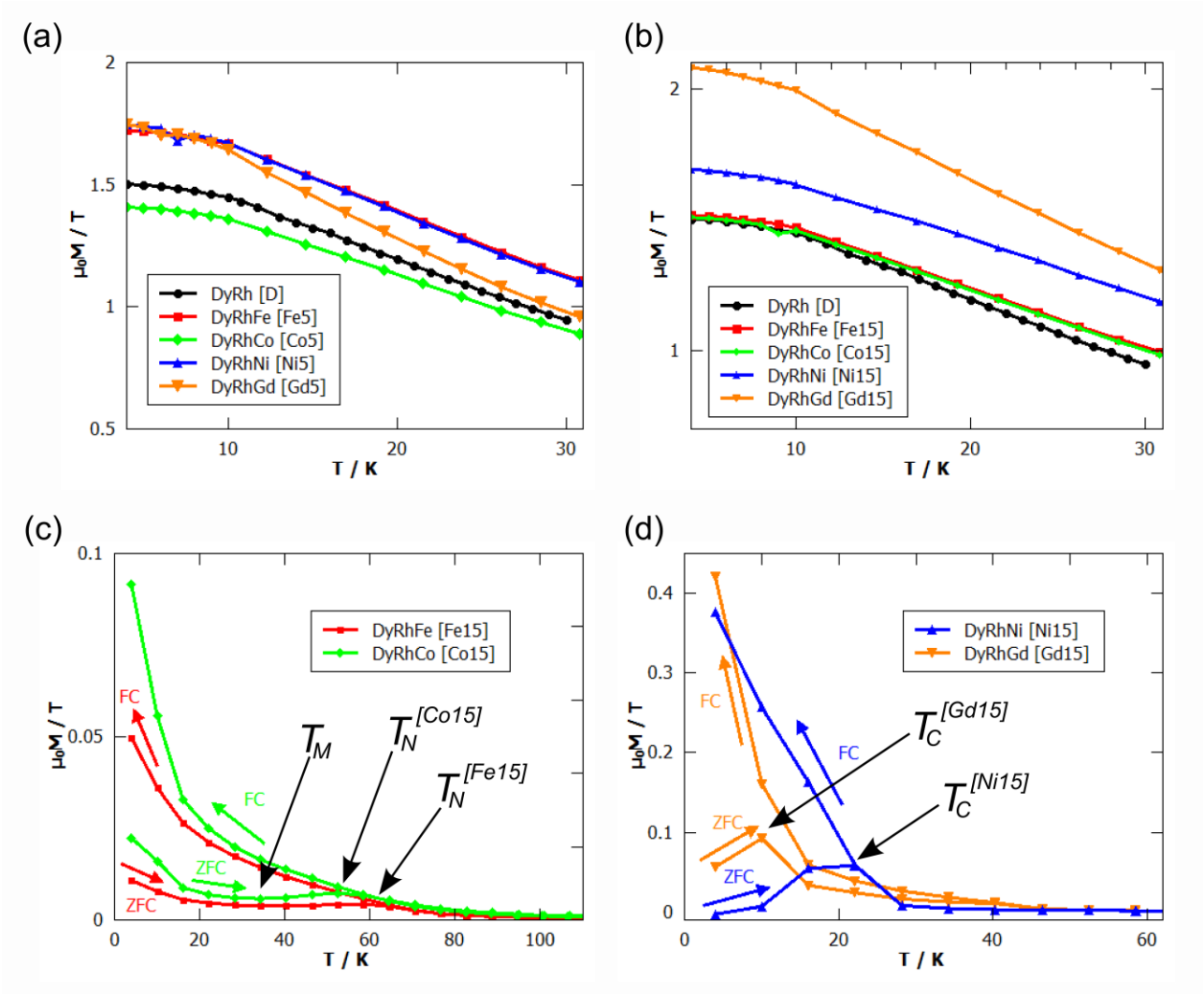
(a)
μ₀M / T
T / K
DyRh [D]
DyRhFe [Fe5]
DyRhCo [Co5]
DyRhNi [Ni5]
DyRhGd [Gd5]
(b)
μ₀M / T
T / K
DyRh [D]
DyRhFe [Fe15]
DyRhCo [Co15]
DyRhNi [Ni15]
DyRhGd [Gd15]
(c)
μ₀M / T
T / K
DyRhFe [Fe15]
DyRhCo [Co15]
FC
ZFC
T_M
$T_N^{[Co15]}$
$T_N^{[Fe15]}$
(d)
μ₀M / T
T / K
DyRhNi [Ni15]
DyRhGd [Gd15]
FC
ZFC
$T_C^{[Gd15]}$
$T_C^{[Ni15]}$